# Fabrication and Characterization of a Miniaturized 15-MHz Side-Looking Phased-Array Transducer Catheter

Nestor E. Cabrera-Munoz, *Member, IEEE*, Payam Eliahoo, Robert Wodnicki, *Member, IEEE,* Hayong Jung, Chi Tat Chiu, Jay A. Williams, Hyung Ham Kim, *Member, IEEE,* Qifa Zhou, *Senior Member, IEEE*, Guang-Zhong Yang, *Fellow, IEEE,* and K. Kirk Shung, *Life Fellow, IEEE*

***Abstract*—This paper describes the development of a miniaturized 15-MHz side-looking phased-array transducer catheter. The array features a 2-2 linear composite with 64 piezoelectric elements mechanically diced into a piece of PMN-30%PT single crystal and separated by non-conductive epoxy kerfs at a 50-µm pitch, yielding a total active aperture of 3.2 mm in the azimuth direction and 1.8 mm in the elevation direction, with an elevation natural focal depth of 8.1 mm. The array includes non-conductive epoxy backing and two front matching layers. A custom flexible circuit connects the array piezoelectric elements to a bundle of 64 individual 48-AWG micro-coaxial cables enclosed within a 1.5-m long 10F catheter. Performance characterization was evaluated via finite element analysis simulations and afterwards compared against obtained measurement results, which showed an average center frequency of 17.7 MHz, an average bandwidth of 52.2% at -6 dB, and crosstalk less than -30 dB. Imaging of a tungsten fine-wire phantom resulted in axial and lateral spatial resolutions of approximately 90 µm and 420 µm, respectively. The imaging capability was further evaluated with colorectal tissue-mimicking phantoms, demonstrating the potential suitability of the proposed phased-array transducer for the intraoperative assessment of surgical margins during minimally invasive colorectal surgery procedures.**

***Index Terms*—Transducer modeling (FEA and analytical), piezoelectric and ferroelectric transducer materials, materials/technology for medical transducers, high-frequency imaging.**

## I. Introduction

MINIMAL access surgery (MAS) has become a popular surgical discipline through which patients undergo reduced trauma and recovery time without compromising the safety and efficacy obtained with traditional open surgery approaches [1]. Due to the minimally invasive access, visualization of the area under treatment becomes a challenge.

Imaging modalities such as magnetic resonance imaging (MRI) and computed tomography (CT) produce good quality images with good contrast resolution and a relatively large field of view; however, a major drawback is that they are not performed intraoperatively since the imaging equipment is bulky and incompatible with the operating theater [2]. As a result, miniaturized interventional devices with imaging capabilities have been developed to fulfill the intraoperative visualization needs of areas undergoing MAS procedures.

Ultrasound imaging is safe and portable with the advantage that the probe itself can be interventional. Interventional ultrasound probes include miniaturized ultrasonic transducers attached to their distal ends. The intended MAS procedures ultimately determine their design requirements such as number of elements, aperture size, frequency, and viewing orientation with their construction presenting a number of technical challenges particularly related to electrical interconnects and packaging [3].

For example, Cummins *et al.* recently developed a miniaturized 60-MHz, side-looking, 64-element, linear array considering required penetration depth and dimensional constraints for a breast biopsy needle [4].

There are also miniaturized probes that combine ultrasound with multiple imaging modalities into a single interventional device. One example developed by Yang *et al.* integrates ultrasound with optical coherence tomography (OCT) and photoacoustic tomography to provide tissue information at different depths and resolutions for ovarian tissue characterization [5].

Furthermore, miniaturized imaging probes have successfully been combined with minimally invasive robotic surgery instruments [6]. One example being developed by the Hamlyn Centre for Robotic Surgery at Imperial College London features an endomicroscopy probe mounted on a novel robotic surgical arm that provides colorectal surgeons with cellular level information at the surface of the colorectal wall undergoing transanal endoscopic microsurgery (TEM) [7].

Manuscript accepted March 15, 2019. This work was supported in part by NIH under Grant P41-EB002182 and in part by UK Engineering and Physical Sciences Research Council (EPSRC). (*Corresponding author: Nestor E. Cabrera-Munoz)*

N. E. Cabrera-Munoz, P. Eliahoo, R. Wodnicki, H. Jung, Q. Zhou, and K. K. Shung are with the Department of Biomedical Engineering, University of Southern California, Los Angeles, CA 90089 USA (e-mail: cabreram@usc.edu)

C. T. Chiu was with the Department of Biomedical Engineering, University of Southern California, Los Angeles, CA 90089 USA. He is now with the Department of Imaging and Bioelectronics, General Electric Global Research, Niskayuna, NY 12309 USA.

J. A. Williams was with the Department of Biomedical Engineering, University of Southern California, Los Angeles, CA 90089 USA.

H. H. Kim was with the Department of Biomedical Engineering, University of Southern California, Los Angeles, CA 90089 USA. He is now with the Department of Creative IT Engineering, Pohang University of Science and Technology, Pohang, Gyeongbuk 37673 South Korea.

G. Z. Yang is with the Hamlyn Centre for Robotic Surgery, Imperial College London, SW7 2AZ, London, UK.

Such robotic surgical arm also enables the integration of a miniaturized endorectal ultrasound (ERUS) probe with a packaging diameter smaller than 3.5 mm to additionally provide depth resolved information below the colorectal wall. However, current commercially available ERUS probes have diameters larger than 15 mm [8].

This paper discusses the fabrication and characterization of a miniaturized 15-MHz, side-looking, 64-element, phased-array transducer packaged within a 10F catheter that can be integrated with the aforementioned robotic surgical instrument. This miniaturized array transducer offers adequate penetration depth and spatial resolutions for its potential application to detect solid structures and cysts present in colorectal tissue.

## II. Array Transducer Design

The side-looking endorectal ultrasound (SL-ERUS) phased-array transducer catheter construction was 3-D modeled via the computer-aided design (CAD) software SolidWorks (Dassault Systèmes SolidWorks Corp., Vélizy-Villacoublay, France) considering dimensional requirements of the robotic surgical instrument. As shown in Fig. 1, such instrument required the array to be enclosed within a 10F catheter having an external diameter of 3.3 mm. The array acoustic stack is connected to a custom flexible circuit that clamps the 2-2 composite on its proximal and distal ends to provide ground connection. The design of the flexible circuit allows connecting and fitting a bundle of 64 individual 48-AWG micro-coaxial cables inside of the catheter to excite each one of the piezoelectric elements. The array does not include a lens to enable colorectal surgeons image the full thickness of the colorectal wall (> 6 mm) [9], while delicately manipulating the instrument within the colorectal cavity.

### A. Array Acoustic Stack

The center frequency of the array was chosen to be 15 MHz to achieve adequate penetration depth and spatial resolutions necessary to reliably visualize the full thickness of the colorectal wall. Lead magnesium niobate-30%lead titanate (PMN-30%PT) (CTS Corporation, Bolingbrook, IL) single crystal was chosen as the piezoelectric material due to its high dielectric constant and low dielectric loss, which make it ideal for high sensitivity transducers with small aperture size [10].

The array 2-2 composite consists of sixty-four 37-µm-wide piezoelectric elements separated by 13-µm-wide kerfs filled with non-conductive epoxy, Epo-Tek 301 (Epoxy Technology, Inc., Billerica, MA), to yield an array with a 50-µm-wide pitch (0.5 $\lambda_{water}$ pitch for the suppression of undesirable grating lobes during beam steering [11]), a total active azimuth aperture of 3.2 mm, and a total active elevation aperture of 1.8 mm with a natural focal distance of 8.1 mm.

The array acoustic stack includes a backing layer of non-conductive epoxy, Epo-Tek 301, mixed with 43.2 wt% liquid plasticizer, LP-3 (Structure Probe, Inc., West Chester, PA), and two front matching layers: 1. Silver-loaded epoxy consisting of 2,3-µm silver powder (Aldrich Chemicals Co., St. Louis, MO) with mixed epoxy, Insulcast 501 + Insulcure 9 (ITW Polymers Coatings North America, Montgomeryville, PA), and 2. Vapor deposited polymer, Parylene C (Specialty Coating Systems, Inc., Indianapolis, IN). The array design parameters and material properties are shown in Table I and Table II, respectively.

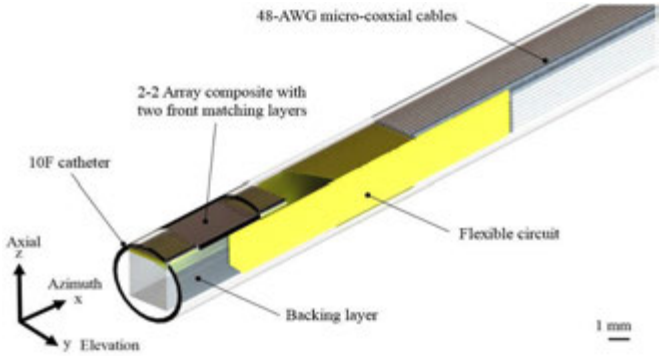


Fig. 1. CAD model of SL-ERUS phased-array transducer enclosed in protective 10F catheter.

TABLE I
SL-ERUS Phased-Array Transducer Design Parameters

| | |
|---|---|
| Design center frequency | 15 MHz |
| Number of elements | 64 |
| Composite configuration | 2-2, linear |
| Pitch | 50 µm (0.5 λwater) |
| Element width | 37 µm |
| Kerf width | 13 µm |
| Elevation aperture | 1.8 mm |
| Azimuth aperture | 3.2 mm |
| Elevation natural focal distance | 8.1 mm |
| Piezoelectric material | PMN-30%PT (53 µm thick) |
| Kerf filler material | Epo-Tek 301 (53 µm thick) |
| Backing layer material | Epo-Tek 301 + 43.2 wt% LP-3 (2 mm thick) |
| 1st Matching layer material | 2,3-µm silver epoxy (45 µm thick) |
| 2nd Matching layer material | Parylene C (30 µm thick) |

### B. Flexible Printed Circuit

The number of elements, their width and pitch, and the available space inside of a 10F catheter required designing a high-density flexible printed circuit. Fig. 2(a) shows the CAD schematics (AutoCAD, Autodesk, Inc., San Rafael, CA) of the flexible circuit design that allows connecting and fitting a bundle of 64 individual 48-AWG micro-coaxial cables inside of the 10F catheter to excite each one of the 64 piezoelectric elements.

The flexible circuit features sixty-four 30-µm-wide signal traces with a 50-µm-wide pitch on the 2-2 array composite area, divided into two groups of 32 signal traces each. Each group further divides into three branches of 10 (center tab) or 11 (side tabs) signal traces, each of which will then be connected to an individual 48-AWG micro-coaxial cable. Connection pads are 100 µm wide and their pitch is 180 µm. Fig. 2(b) shows the folding sequence of the flexible circuit: 1. Flat state, 2-3. Fold composite clamping flaps, 4. Fold two main branches, 5. Fold side tabs of first main branch, and 6. Fold side tabs of second main branch.

This article has been accepted for publication in a future issue of this journal, but has not been fully edited. Content may change prior to final publication. Citation information: DOI 10.1109/TUFFC.2019.2906134, IEEE Transactions on Ultrasonics, Ferroelectrics, and Frequency Control



TABLE II
MATERIAL PROPERTIES OF THE SL-ERUS PHASED-ARRAY TRANSDUCER ACOUSTIC STACK

| Material | PMN-30%PT single crystal[1] | Epo-Tek 301[2] | Epo-Tek 301 + 43.2 wt% LP-3[3] | 2,3-µm silver epoxy[3] | Parylene C[4] |
|---|---|---|---|---|---|
| Density, $\rho$ (kg/m$^3$) | 7,800 | 1,150 | 1,230 | 3,860 | 1,100 |
| Acoustic longitudinal velocity, $c$ (m/s) | 4,600 | 2,650 | 2,450 | 1,900 | 2,350 |
| Acoustic impedance, $Z$ (MRayl) | 35.88 | 3.05 | 3.01 | 7.33 | 2.59 |
| Piezoelectric strain constant, $d_{33}$ (C/N) | 1,500 x $10^{-12}$ | - | - | - | - |
| Free dielectric constant, $K^{\kappa}$ | ~5,000 | - | - | - | - |
| Clamped dielectric constant, $K^{\varepsilon}$ | 800 | - | - | - | - |
| Dielectric loss tangent, tan$\delta_e$ | 0.005 | - | - | - | - |
| Electromechanical coupling coefficient, $k_t$ | 0.58 | - | - | - | - |

1. CTS Corporation, Bolingbrook, IL
2. Epoxy Technology, Inc., Billerica, MA
3. Resource Center for Medical Ultrasonic Transducer Technology at the University of Southern California, Los Angeles, CA
4. Specialty Coating Systems, Inc., Indianapolis, IN

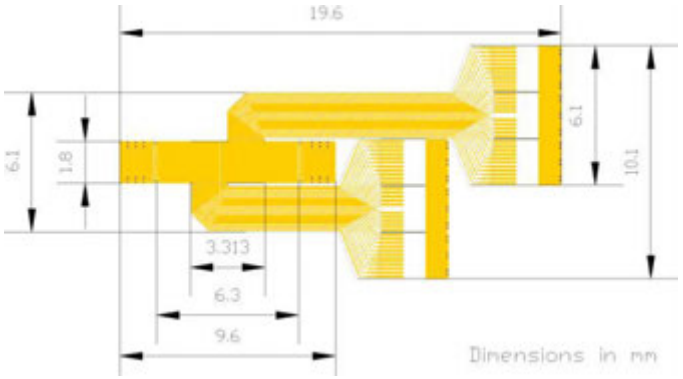


(a)

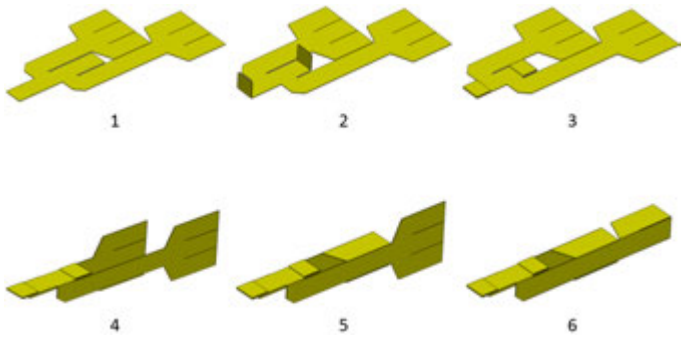


(b)

Fig. 2. (a) CAD schematics of flexible printed circuit design. (b) Folding sequence of the flexible printed circuit.

### C. Micro-Coaxial Cable

The micro-coaxial bundle features 64 individual 48-AWG micro-coaxial cables (#5481-120, Hitachi Metals, Ltd., Tokyo, Japan). The micro-coaxial cable was first characterized to determine its impedance, $Z_o$, and propagation constant, γ, at 15 MHz based upon the following formula for a micro-coaxial cable of length $x$ [12]:

$$Z_x = Z_o \frac{[Z_{load} + Z_o \tanh(\gamma x)]}{[Z_o + Z_{load} \tanh(\gamma x)]} \quad (1)$$

where $Z_{load}$ represents the electrical impedance of the transducer and $Z_x$ is the transformed coaxial impedance measured on the system end of the cable. The values for $Z_o$ and $\gamma$ were obtained by measuring the complex open and short-circuit impedance for a sample cable on an Agilent E4991A RF Impedance/Material Analyzer (Agilent Technologies, Santa Clara, CA). As done by Cannata *et al.,* the complex transformed impedance was recorded for both the short-circuit and the open-circuit $Z_{laod}$ values [13]. The two measured values for $Z_x$ and equation (1) were then used to solve for $Z_o$ and $\gamma$. The distributed network representation for the micro-coaxial cable was also solved [14]. The resultant per-unit-length values of cable propagation velocity ($v$), DC resistance ($r$), series inductance ($l$), shunt capacitance ($c$), and attenuation (α) were recorded and are listed in Table III.

TABLE III
MEASURED PROPERTIES OF THE 48-AWG MICRO-COAXIAL CABLE AT 15 MHZ

| Property | Hitachi #5481-120 | | |
|---|---|---|---|
| Characteristic impedance, $Z_o$ | 52.59 - 22.63i Ω | | |
| Propagation constant, $\gamma$ | 0.24 + 0.57i m$^{-1}$ | | |
| Propagation velocity, $v$ | 1.6 x $10^8$ m/s | | |
| DC resistance / unit length, $r$ | 21.3 Ω/m | | |
| Series inductance / unit length, $l$ | 0.12 µH/m | | |
| Shunt capacitance / unit length, $c$ | 127 pF/m | | |
| Attenuation / unit length, $\alpha$ | 2.08 dB/m | | |
| | 1.5 m | 2.0 m | 2.4 m |
| Reflection coefficient, $S_{11}$ (dB) | -11.56 | -11.01 | -10.99 |
| Transmission coefficient, $S_{21}$ (dB) | -3.18 | -4.21 | -5.08 |

In order to determine the optimal micro-coaxial cable length to be used, scattering parameters (S-Parameters) were evaluated to achieve the best performance in terms of reflection and transmission [15].

The S-Parameters of the 48-AWG micro-coaxial cable were measured at three different cable lengths considering minimum and maximum cable length requirements provided by the Hamlyn Centre for Robotic Surgery. Measurements were performed under no-load conditions, with the micro-coaxial cable connected to the two 50-Ω ports of an Agilent E5072A Network Analyzer (Agilent Technologies, Santa Clara, CA). Table III shows the effect of the micro-coaxial cable length on the S-Parameters. At 15 MHz the reflection coefficient, $S_{11}$, increases with increasing cable length. 1.5-m cable length generates less reflection at the input and output; therefore

This article has been accepted for publication in a future issue of this journal, but has not been fully edited. Content may change prior to final publication. Citation information: DOI 10.1109/TUFFC.2019.2906134, IEEE Transactions on Ultrasonics, Ferroelectrics, and Frequency Control



having less oscillatory effect on the transmitted and received signal. At 15 MHz the transmission coefficient, $S_{21}$, decreases with increasing cable length. In other words, the loss of transmitted signal increases with increasing cable length. Therefore, the measurements denote what is expected from a lossy transmission line model and clearly indicate that 1.5-m cable length delivers higher power to the drive the array transducer.

### D. *Array Transducer Simulation Modeling*

The SL-ERUS phased-array transducer was simulated via a 2-D finite-element-analysis (FEA) model (PZFlex, Weidlinger Associates, Inc., Cupertino, CA) to predict its performance and therefore reduce the number of time-consuming prototype fabrication runs [16]. The array performance was evaluated and optimized via standard non-imaging simulations that included electrical impedance, pulse-echo response, as well as combined electrical and acoustical crosstalk. Fig. 3 shows a section of the FEA model illustrating the simulated layers. The Field II program was used to simulate the one-way azimuthal directivity response of a single array element [17] and to estimate the effective element width. KLM modeling (PiezoCAD, Sonic Concepts, Inc., Bothell, WA) was used to simulate the insertion loss of a single array element. Comparisons of simulated results against measured results are presented below in section VI. RESULTS AND DISCUSSION.

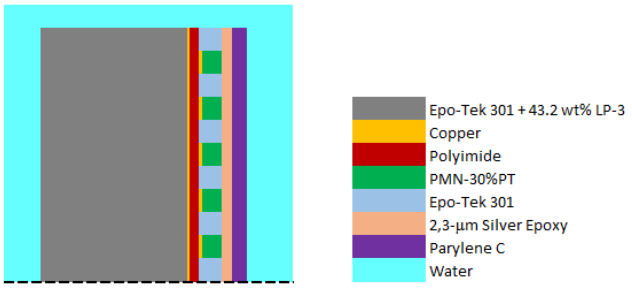


Fig. 3. Section of the FEA model illustrating the simulated layers.

## III. Array Transducer Fabrication

### A. *Array Acoustic Stack*

The array 2-2 composite was fabricated using the dice-and-fill technique described by Savakus *et al.* [18]. At CTS Corporation (CTS Corporation, Bolingbrook, IL) kerfs were mechanically cut with a dicing saw (0.5 mm/s feed rate and 40,000 RPM spindle speed) into a plate of bulk PMN-30%PT and backfilled with Epo-Tek 301 epoxy. The diced-and-filled PMN-30%PT plate was then shipped to our group, the Resource Center for Medical Ultrasonic Transducer Technology at the University of Southern California. One of its sides was then lapped down using 2,000-grit sandpaper together with 9-µm aluminum oxide ($Al_2O_3$) powder (Buehler-Illinois Tool Works, Inc., Lake Bluff, IL) to ensure a smooth, matte finish. Lapping with 9-µm diamond suspension, MetaDi (Buehler-Illinois Tool Works, Inc., Lake Bluff, IL), was done at the end to remove any excess of kerf filler epoxy and make sure that the whole first lapped side of the piece was completely flat.

Afterwards, the sample was mechanically cleaned by applying acetone, reagent alcohol, and Alconox detergent (Alconox, Inc., White Plains, NY) with a cotton swab and any residues left were removed with deionized water. The lapped and mechanically cleaned side of the 2-2 composite was then plasma cleaned (argon 25 sccm, 30 watts, 185 s) to activate the exposed surface of the piezoelectric elements for electroplating sputtering of their active electrodes having a thickness of 500 Å of chrome and 2,000 Å of gold. Since electroplating sputtering actually covered the whole top surface of the 2-2 composite, the active electrodes were patterned on the piezoelectric elements by removing gold and chrome from the epoxy kerfs with a cotton swab dampened in reagent alcohol, taking advantage of the weak adhesion of chrome and gold to epoxies.

The 2-2 composite was then flipped over and lapped down to its final design thickness. Again, 2,000-grit sandpaper together with 9-µm $Al_2O_3$ powder were used to ensure a smooth, matte finish and 9-µm diamond suspension lapping was done to remove any excess of kerf filler epoxy. After undergoing the same process of mechanical and plasma cleaning, the 2-2 composite had its common ground sputtered having a thickness of 500 Å of chrome and 2,000 Å of gold.

The 1st matching layer was then prepared by adding 4.5 gr of 2,3-µm silver powder to 1.25 gr of mixed non-conductive epoxies Insulcast 501 and Insulcure 9. The resulting mixture was then degassed to avoid the presence of air bubbles, cast on top of the common ground electrode, and centrifuged at 3,000 RPM for 15 mins to distribute it evenly. After curing overnight in a dry-environment nitrogen box and post-curing in a forced convection oven for 2 hrs at 45 °C, the 1st matching layer was lapped down to its final design thickness and the resulting acoustic stack (2-2 composite + 1st matching layer) was mechanically diced (0.5 mm/s feed rate and 30,000 RPM spindle speed) to final dimensions as shown in Fig. 4.

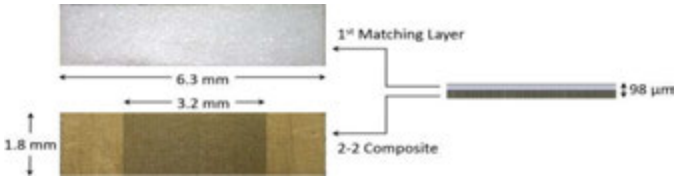


Fig. 4. Acoustic stack comprising the PMN-30%PT 2-2 composite and 1st matching layer. Active and ground electrodes were sputtered on the bottom and top sides of the composite, respectively. Both layers were lapped down to final design thicknesses and the resulting stack was mechanically diced to final dimensions.

### B. *Flexible Printed Circuit*

The two-layer flexible printed circuit was fabricated by MicroConnex (MicroConnex Corp., Snoqualmie, WA). Fig. 5 shows a physical sample of the flexible circuit consisting of a 25-µm-thick base dielectric polyimide layer, Kapton (DuPont, Wilmington, DE), which features signal traces on the front (cover-layer protected along the main branches) and an exposed common ground electrode on the back with etched transparent windows that reveal the polyimide layer for 2-2 composite proper alignment and positioning. All signal traces and ground

This article has been accepted for publication in a future issue of this journal, but has not been fully edited. Content may change prior to final publication. Citation information: DOI 10.1109/TUFFC.2019.2906134, IEEE Transactions on Ultrasonics, Ferroelectrics, and Frequency Control



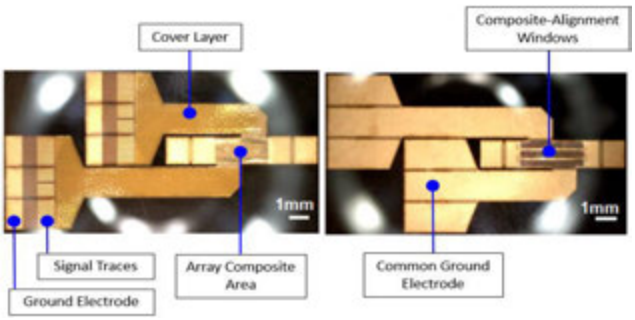


(a) (b)

Fig. 5. Flexible printed circuit for the SL-ERUS phased-array transducer. (a) Front side with cover-layer protected signal traces. (b) Back side with exposed common ground electrode featuring three windows for 2-2 composite proper alignment and positioning.

electrodes were patterned over a 4-µm-thick copper layer and finished with a flash of gold.

### *C. Assembling the Array Acoustic Stack – Flexible Printed Circuit – Backing Layer Module*

After mechanical dicing to final dimensions, both sides of the resulting array acoustic stack were cleaned by applying trichloroethylene, acetone, and reagent alcohol with a cotton swab. Likewise, the front side of the flexible circuit was cleaned with a cotton swab dampened in reagent alcohol. Afterwards, a thin line of Epo-Tek 301 epoxy was applied with a foam swab at the center of the flexible circuit, on the 2-2 composite area. Another foam swab was used then to smear a thin layer of Epo-Tek 301 epoxy all over the surface of the 2-2 composite (bottom side of the array acoustic stack).

The acoustic stack was afterwards placed on top of the flexible circuit visually making sure that the piezoelectric elements were correctly aligned with the signal traces, and pressure was applied using a "C" clamp. The resulting sub-assembly was cured overnight in a dry-environment nitrogen box and then post-cured in a forced convection oven for 2 hrs at 45 °C.

The next step involved bonding the backing layer to the backside of the flexible circuit. For this purpose, the backside of the flexible circuit was cleaned with a cotton swab dampened in reagent alcohol. Afterwards, a thin line of Epo-Tek 301 epoxy was applied with a foam swab at the center of the flexible circuit (backside of the 2-2 composite area) and another foam swab was used then to smear a thin layer of Epo-Tek 301 epoxy all over the bonding surface of the backing layer. The backing layer was afterwards placed on top of the flexible circuit backside and pressure was once again applied with a "C" clamp. Likewise, the resulting sub-assembly was cured overnight in a dry-environment nitrogen box and then post-cured in a forced convection oven for 2 hrs at 45 °C.

In order to connect the common ground electrode on the backside of the flexible circuit to the front matching layer, the two clamping flaps featuring metallized thru-vias were bent and then bonded to the front matching layer using conductive epoxy, E-Solder 3022 (Von Roll Isola USA, Inc., Schenectady, NY). Afterwards, the two main branches of the flexible circuit were bent and bonded to the sides of the backing layer using Epo-Tek 301 epoxy.

The resulting module was then all covered, excluding the soldering pads, with a 30-µm-thick layer of vapor deposited polymer, Parylene C, serving as both the 2nd matching layer and insulation. Fig. 6 shows cross-sectional images revealing the diverse components of the assembled module and a detail view of the bending of one main branch of the flexible circuit, making sure there were no broken signal traces.

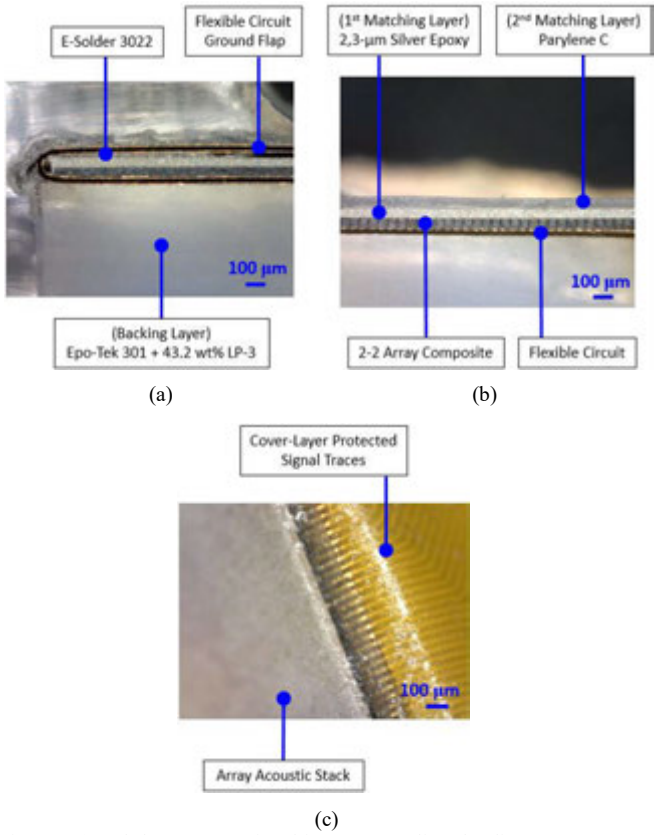


(a) (b)

(c)

Fig. 6. (a) and (b) Cross-sectional images revealing the diverse components of the array acoustic stack and backing layer bonded to the flexible circuit. (c) Detail view of the bending of one main branch of the flexible circuit, making sure there were no broken signal traces.

### *D. Micro-Coaxial Cable-Assembly Connection to the Flexible Printed Circuit*

The 48-AWG micro-coaxial cable was cut into sixty-four 1.5-m long pieces with their ends codified with colors and a corresponding number, respectively. Afterwards, all the 64 pieces were carefully pulled through a 1.45-m long 10F PTFE catheter and had their color ends manually stripped.

The exposed inner conductor of each single piece of 48-AWG micro-coaxial cable was then carefully bonded to its respective 100-µm-wide connection pad using E-Solder 3022 epoxy. After completing the first side with the first 32 connections, Epo-Tek 301 epoxy was manually applied over the three flexible circuit tabs to pot and protect the connections created. More E-Solder 3022 epoxy was then manually applied to bond the exposed outer conductors to the ground pads of each of the three flexible circuit tabs. The same process was repeated for the second side with the remaining 32 connections. Fig. 7(a) shows a picture of all 64 connections completed.

For larger scale manufacturing, resistance welding with parallel-gap fine tip could be implemented to expedite soldering of the micro-coaxial cable assembly to the flexible circuit.

This article has been accepted for publication in a future issue of this journal, but has not been fully edited. Content may change prior to final publication. Citation information: DOI 10.1109/TUFFC.2019.2906134, IEEE Transactions on Ultrasonics, Ferroelectrics, and Frequency Control



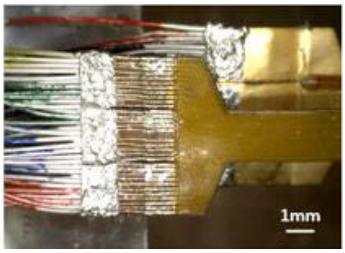


(a)


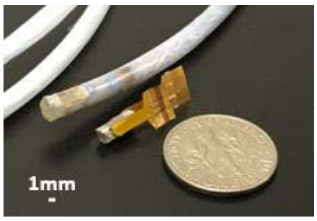


(b) (c)

Fig. 7. (a) Connection of the 48-AWG micro-coaxial cable assembly to the flexible printed circuit. (b) Finished distal end with 7-µm-thick layer of vapor deposited Parylene C to ensure complete insulation. (c) Size comparison of the finished distal end, the array acoustic stack-flexible circuit-backing layer module, and a dime coin.

Furthermore, flexible transmission lines on liquid crystal polymer (LCP) offering comparable signal integrity to micro-coaxial cable could also be developed and be brought down the length of the catheter [19].

### *E. Final Packaging and Connection to Imaging System Connector*

After completing all connections, the flexible circuit was folded into its final configuration and carefully pulled inside the distal end of the 10F PTFE catheter. The array aperture was then positioned right in the center of a manually pre-cut window (3.7 mm x 2.2 mm) on the distal end of the catheter. Epo-Tek 301 epoxy was applied to fill in the gaps between the array acoustic stack-flexible circuit-backing layer module and the edges of the window, as well as to seal the opening at the tip of the catheter.

Afterwards, a 7-µm-thick layer of Parylene C was vapor deposited to ensure complete insulation of the distal end of the SL-ERUS phased-array transducer catheter as shown in Fig. 7(b). A size comparison of the distal end of the SL-ERUS phased-array transducer catheter, the array acoustic stack–flexible circuit–backing layer module, and a dime coin is shown in Fig. 7(c).

The proximal end of the cable assembly was then connected with E-Solder 3022 epoxy to a pair of Verasonics micro-coax termination boards (Verasonics, Inc., Kirkland, WA), each one handling 32 micro-coaxial cables. All the connections were potted with Epo-Tek 301 epoxy for protection, leaving exposed just the top surface of the resulting E-Solder 3022 epoxy electrodes for posterior poling and testing. Fig. 8(a) shows the two bundles of 32 micro-coaxial cables, each held together with a piece of polyimide tape, bonded with Epo-Tek 301 epoxy to a black PVC cable-strain relief boot (Amphenol Corporation, Wallingford, CT), and finished with a Verasonics M14-A2-70 Hex cable-strain relief nut.

The pair of Verasonics micro-coax termination boards were then connected to a Verasonics Backshell Connector, following Verasonics channel mapping to avoid any drawback when connecting the array transducer to a Verasonics Vantage imaging system. Fig. 8(b) shows the completely finished SL-ERUS phased array transducer catheter.

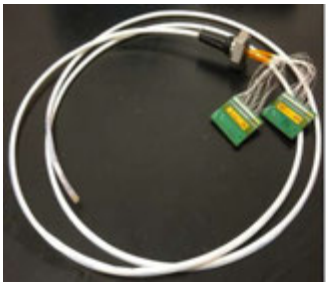

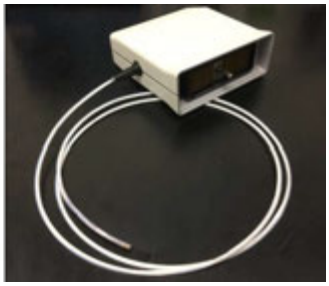

(a) (b)

Fig. 8. (a) SL-ERUS phased-array transducer finished with a pair of Verasonics micro-coax termination boards, each one handling 32 channels. (b) SL-ERUS phased-array transducer connected to Verasonics Backshell Connector.

## IV. Array Transducer Characterization

### *A. Electrical Impedance*

Before connecting the array acoustic stack – flexible circuit – backing layer module to the micro-coaxial cable assembly, each one of the 64 piezoelectric PMN-30%PT elements was individually re-polarized in air at room temperature under an electric field of 20 kV/cm for 3 mins using a Spellman-Bertan Model 210-02R high voltage power supply (Spellman High Voltage Electronics Corporation, Hauppauge, NY). The electrical impedance of each individual array element was then measured using its respective flexible circuit signal and ground electrodes as probing pads with an Agilent E4991A RF Impedance/Material Analyzer (Agilent Technologies, Santa Clara, CA) and both magnitude and phase angle were recorded over the frequency range of the array transducer pass-band.

### *B. Pulse-Echo Response and Insertion Loss*

Upon fabrication completion of the SL-ERUS phased-array transducer catheter, the 64 piezoelectric PMN-30%PT elements were once again individually re-polarized under the same aforementioned conditions. Afterwards, the pulse-echo response of each individual array element was recorded to determine its effective center frequency, -6 dB fractional bandwidth, peak-to-peak sensitivity, and pulse length.

This test was performed by immersing the SL-ERUS phased-array transducer catheter in a deionized water tank containing a polished quartz reflector as the target at the elevation natural focal distance of 8.1 mm. The pulser/receiver used was a Panametrics – NDT 5900PR (Panametrics, Inc., Waltham, MA), which emitted single cycle unipolar pulses with an amplitude of -100 V at a pulse repetition frequency (PRF) of 200 Hz. Energy and damping were set at 1 µJ and 50 Ω, respectively. To receive echo signals, the Panametrics – NDT 5900PR was set with a bandpass filter from 10 MHz to 20 MHz and a gain of 40 dB, which were applied before analog signals were digitized via a GaGe EON CompuScope CS122G1 Digitizer (Dynamic Signals, LLC, Lockport, IL) with a 1-GS/s sampling rate.

Insertion loss was measured by immersing the SL-ERUS phased-array transducer catheter in a deionized water tank, exciting each element in the array with a 5-Vpp, 30-cycle

sinusoidal tone-burst signal generated by a Tektronix AFG 3252 Dual Channel Arbitrary / Function Generator (Tektronix, Inc., Beaverton, OR) at the array center frequency, and receiving the reflected echo from a polished quartz reflector placed at the elevation natural focal distance. Measured echo signals were divided by the input signal and the resulting quotients were expressed in decibels. Afterwards, these results were corrected for loss due to attenuation in water ($\alpha$ = 2.0 x $10^{-4}$ dB/mm-MHz$^2$) and reflection from the quartz target (1.9 dB) [13], [20].

### C. Combined Electrical and Acoustical Crosstalk

Combined electrical and acoustical crosstalk measurements were performed by immersing the SL-ERUS phased-array transducer catheter in a deionized water tank with no polished quartz reflector. A Tektronix AFG 3252 Dual Channel Arbitrary / Function Generator was used to excite one element in the array with a 5-Vpp, 5-cycle sinusoidal tone-burst signal within a frequency range from 2 MHz to 30 MHz in steps of 2 MHz. The applied signal was measured with a LeCroy LC534 1-GHz Oscilloscope (LeCroy Corporation, Chestnut Ridge, NY) and served as a reference to the measured signals from four adjacent elements. These measurements were executed on element 18 with respective adjacent elements 17, 16, 15, and 14 as well as on element 37 with respective adjacent elements 36, 35, 34, and 33. Afterwards, the crosstalk for first adjacent elements, second adjacent elements, third adjacent elements, and fourth adjacent elements were averaged and plotted as relative amplitudes.

### D. Single-Element Azimuthal Directivity Response

The one-way azimuthal directivity response was measured by exciting a representative array element with a 50-Vpp, 5-cycle sinusoidal tone-burst signal generated by a Tektronix AFG 3252 Dual Channel Arbitrary / Function Generator connected to an Amplifier Research 50W1000B solid-state power amplifier (Amplifier Research, Inc., Souderton, PA). A needle hydrophone HGL-0085 (Onda Corporation, Sunnyvale, CA), placed at the natural elevation focus and connected to a LeCroy WaveRunner 104MXi 1-GHz Oscilloscope, was used to acquire the amplitude of the time-domain response at discrete angular positions. The effective element width was estimated by matching a theoretical directivity curve to the measured values [13], [21].

## V. Array Transducer Imaging

The ultimate performance indicators of the SL-ERUS phased-array transducer catheter were determined by its imaging capability of three different kinds of targets using a Verasonics Vantage 128 System.

Imaging was performed acquiring 128 ray lines in a phased-array configuration, with each ray line constituting a separate beamformed transmit operation with fixed focus, followed by a respective beamformed receive operation with dynamic focusing, yielding 128 transmit and receive angles spaced at ($\pi$/2)/128.

RF data was acquired at a sampling frequency of 62.5 MHz, with the transmit frequency set to 15.625 MHz, and a three-half-cycle-pulse transmit waveform.

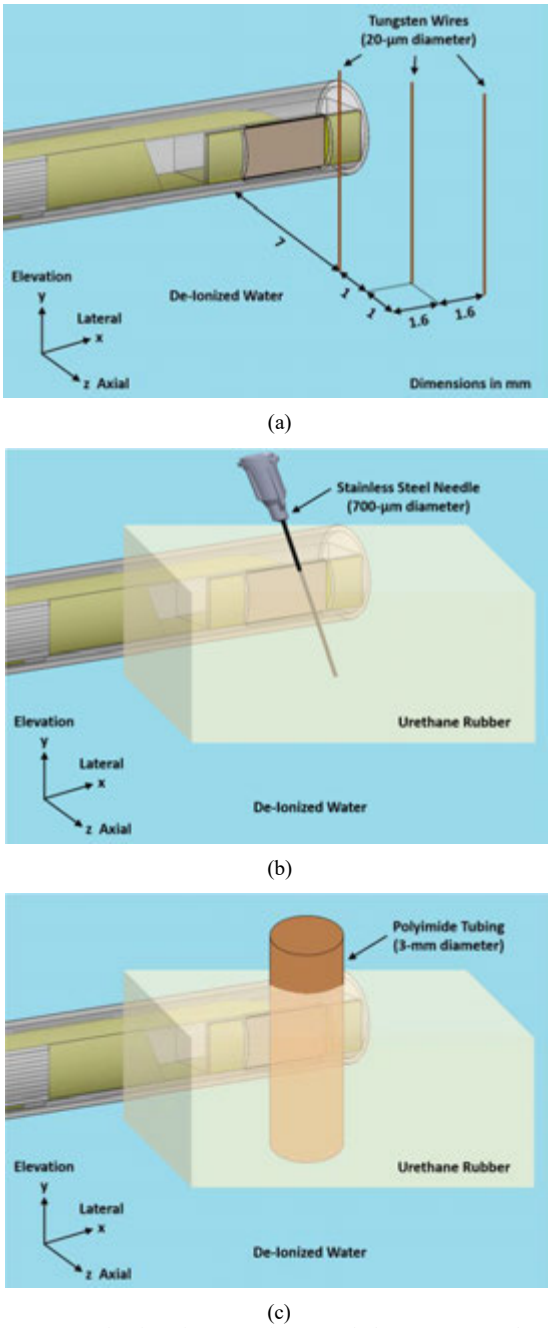


Fig. 9. Targets for imaging experiments of the SL-ERUS phased-array transducer catheter. (a) Custom-made fine-wire phantom. (b) Custom-made colorectal tissue-mimicking phantom with inserted 700-µm-diameter stainless steel needle. (c) Custom-made colorectal tissue-mimicking phantom with inserted piece of 3-mm-diameter polyimide tubing. All targets were immersed in a tank with deionized water during the imaging experiments.

After all of the individual ray lines were acquired, the image data was reconstructed to yield the phased-array images. The system 40-dB TGC was adjusted to optimize the images for display. No apodization was applied to the array transducer aperture in any of the imaging experiments.

The first target, shown in Fig. 9(a), was a custom-made fine-wire phantom composed of three evenly spaced 20-µm-diameter tungsten wires (California Fine Wire Company, Grover Beach, CA) with the purpose of determining the axial and lateral spatial resolutions of the array transducer. The axial separation between wires was around 1.0 mm and the azimuth

separation was around 1.6 mm. The custom-made fine-wire phantom was immersed in a tank with deionized water. At a center frequency of 15 MHz, the sound wavelength in the transmitting medium is 100 μm; therefore, the wires could safely be assumed as three point targets. The transmit focus was set at a depth of 8 mm with a transmit pulse of 40 Vpp. The acquired image was post-processed with a scaling gain of 15 dB and minimal thresholding was used in order to highlight the wire targets.

The second target, shown in Fig. 9(b), was a custom-made colorectal tissue-mimicking phantom composed of urethane rubber ($\alpha$ = 0.5 dB/cm-MHz, $c$ = 1,450 m/s) (Supertech, Inc., Elkhart, IN) into which a 700-μm-diameter stainless steel needle was inserted with the purpose of demonstrating the capability of the array transducer to detect solid structures embedded in tissue. The custom-made colorectal tissue-mimicking phantom was immersed in a tank with deionized water. The transmit focus was set at a depth of 12 mm with a transmit pulse of 40 Vpp. The acquired images were post-processed with a scaling gain of 26 dB.

The third and last target, shown in Fig. 9(c), was a custom-made colorectal tissue-mimicking phantom composed of urethane rubber into which a piece of 3-mm-diameter polyimide tubing was inserted with the purpose of demonstrating the capability of the array transducer to detect cysts present in tissue. The custom-made colorectal tissue-mimicking phantom was immersed in a tank with deionized water. The transmit focus was set at a depth of 6 mm with a transmit pulse of 40 Vpp. The acquired images were post-processed with a scaling gain of 22 dB.

## VI. Results and Discussion

### A. Electrical Impedance

The simulated and measured electrical impedance magnitude and phase angle of a representative array element (element 33) are shown in Fig. 10(a). Element 33 was chosen as representative since its electrical impedance characteristics were closest to the average of all 64 elements.

The simulated and measured results are summarized and compared in Table IV. The measured results showed an electrical impedance magnitude of 129.6 ± 25.3 Ω at 15 MHz. The series ($f_r$) and parallel ($f_a$) resonant frequencies were 16.9 ± 1.5 MHz and 20.4 ± 1.8 MHz, respectively, yielding an electromechanical coupling coefficient ($k_t$) of 0.60 ± 0.08 and determined according to the expression [22]:

$$k_t = \sqrt{\frac{\pi}{2}\frac{f_r}{f_a}\tan\left[\frac{\pi}{2}\left(\frac{f_a - f_r}{f_a}\right)\right]} \qquad (2)$$

The uniformity of the measured values of electrical impedance magnitude and phase angle of all the array elements at 15 MHz is shown in Fig. 10(b). As it can be seen, only four elements presented a short circuit to ground: 42, 54, 55, and 64. The average and standard deviation of the array elements electrical impedance magnitude and phase angle were (129.6 ± 25.3 Ω) and (-33.2 ± 6.1°), respectively.

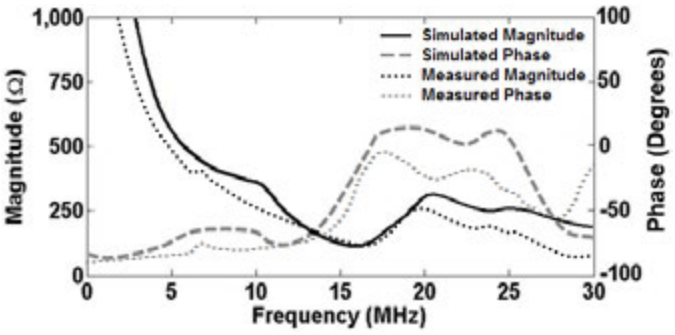


(a)

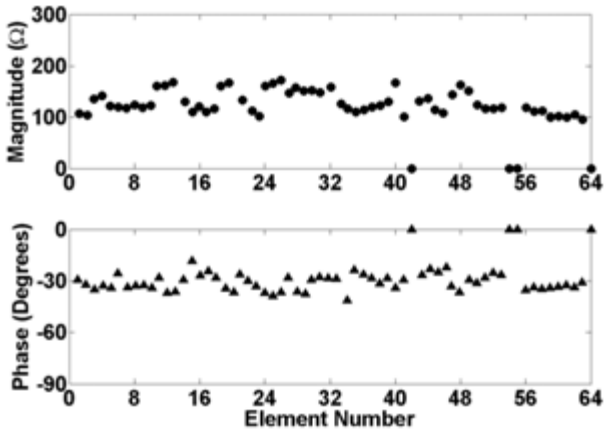


(b)

Fig. 10. (a) Simulated and measured electrical impedance magnitude and phase angle of representative array element 33. (b) Uniformity of electrical impedance magnitude and phase angle of all the phased-array elements.

TABLE IV
Comparison of Simulated and Measured Electrical Impedance Results

| Parameter | PZFlex | Measured |
|---|---|---|
| $Z$@ 15 MHz (Ω) | 124.1 | 129.6 ± 25.3 |
| $f_r$ (MHz) | 16.1 | 16.9 ± 1.5 |
| $f_a$ (MHz) | 19.8 | 20.4 ± 1.8 |
| $k_t$ | 0.62 | 0.60 ± 0.08 |

### B. Pulse-Echo Response and Insertion Loss

The simulated and measured pulse-echo response of a representative array element (element 37) are shown in Figs. 11(a) and 11(b), respectively. Element 37 was chosen as representative since its pulse-echo response characteristics were closest to the average of all 64 elements.

The simulated and measured results are summarized and compared in Table V. The measured results showed an effective -6 dB center frequency (-6 dB fc) of 17.7 ± 1.2 MHz, a -6 dB fractional bandwidth (-6 dB BW) of 52.2 ± 9.8%, a peak-to-peak sensitivity (Vpp) of 200.1 ± 102.7 mV, and a compensated insertion loss (IL) of 49.8 ± 3.9 dB.

The increase of center frequency resulted from slightly over lapping the 2-2 composite by hand, which consequently resulted in shorter -6 dB / -20 dB pulse lengths. The slight decrease in sensitivity resulted mainly from the array elements not having their entire bottom surface perfectly connected to their respective electrodes on the flexible circuit, as it was the

This article has been accepted for publication in a future issue of this journal, but has not been fully edited. Content may change prior to final publication. Citation information: DOI 10.1109/TUFFC.2019.2906134, IEEE Transactions on Ultrasonics, Ferroelectrics, and Frequency Control



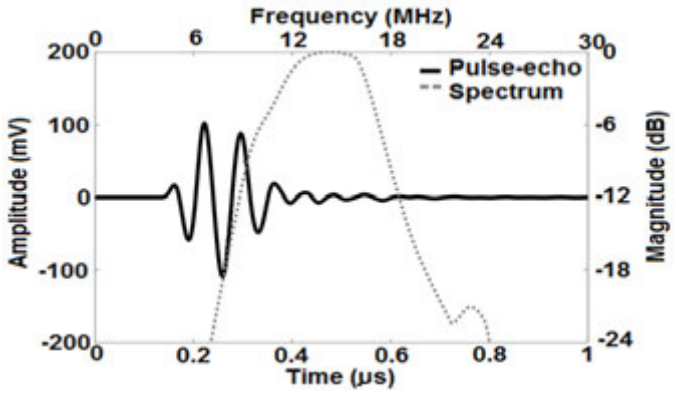


(a)

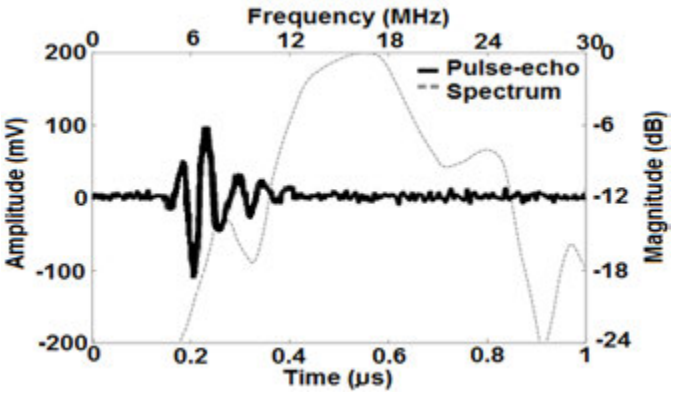


(b)

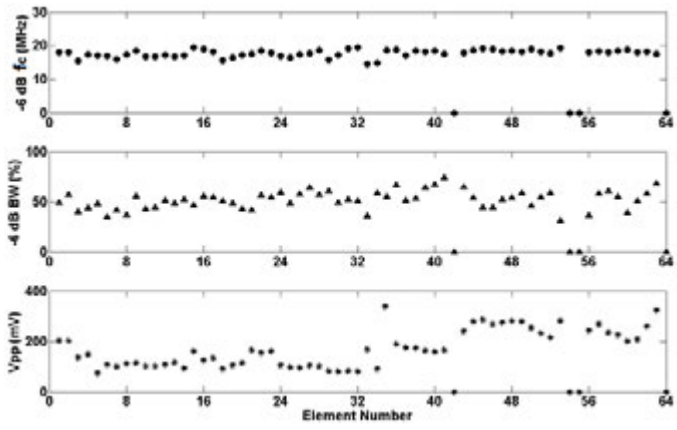


(c)

Fig. 11. (a) Simulated and (b) measured pulse-echo response of representative array element 37. (c) Uniformity of -6 dB center frequency, -6 dB fractional bandwidth, and peak-to-peak sensitivity of all the phased-array elements.

TABLE V
COMPARISON OF SIMULATED AND MEASURED PULSE-ECHO RESPONSE RESULTS

| Parameter | PZFlex | Measured |
|---|---|---|
| -6 dB fc (MHz) | 14.2 ± 0.7 | 17.7 ± 1.2 |
| -6 dB BW (%) | 54.3 ± 3.1 | 52.2 ± 9.8 |
| Vpp (mV) | 211.3 ± 95.8 | 200.1 ± 102.7 |
| -6 dB / -20 dB pulse length (ns) | 135 / 210 | 107 / 193 |
| Compensated IL (dB)* | 41.7 | 49.8 ± 3.9 |

*Simulated value obtained with KLM modeling for a single array element.

case of the FEA simulation model. In reality, the resulting Epo-Tek 301 epoxy thin bonding layer was not perfectly uniform after the clamping process. This can be verified by closely examining the cross-sectional image of the array acoustic stack shown in Fig. 6(b) and by observing the peak-to-peak sensitivity uniformity shown in Fig. 11(c), which clearly indicates how the second half of the array (elements 33 to 64) was better connected to the flexible printed circuit by showing higher peak-to-peak sensitivities than the first 32 elements.

The measured compensated insertion loss was higher than that reported for other linear phased arrays with similar construction; however, the element footprint and, consequently, the dimensions of the signal electrodes on the flexible printed circuit in this array were at least 2 times smaller, making it more difficult to ensure a perfect connection between the bottom surface of the array elements and their respective flexible circuit signal electrodes. For example, the side-looking phased-array transducer developed by Stephens *et al.* [23] featured 64 elements within an aperture of 2.6 mm by 6.4 mm, at a pitch of 100 μm, and a center frequency of 7.25 MHz; whereas the side-looking phased-array transducer being presented includes the same number of elements within an aperture of 1.8 mm by 3.2 mm, at a pitch of only 50 μm, and a center frequency of 17.7 MHz.

Additionally, the 64 individual 48-AWG micro-coaxial cables used in the array under discussion were not shielded as a bundle, making them more susceptible to external noise and interference considering that the outer conductor thickness of each micro-coaxial cable is 17 μm and the skin depth of copper at 15 MHz is approximately 16.8 μm. For good shielding effect, the thickness of the outer conductor should be at least five times greater than the skin depth [24]. A solution could be to assemble all 64 micro-coaxial cables together with 50-μm binder tape, shield them with 46-AWG braiding, and wrap them with 50-μm fluoropolymer tape [23]. This additional shielding would prevent electromagnetic wave radiation through the outer conductor of each micro-coaxial cable; therefore decreasing insertion loss and improving sensitivity by preserving the signal integrity of the received echo.

To obtain acceptable SNR in tissue, future versions of the catheter could include impedance transformers or active pre-amplifiers on each channel, which are commonly used to boost the signal above the noise floor of the system for small elements with high impedance [25]. The uniformity of the measured values of -6 dB center frequency, -6 dB fractional bandwidth, and peak-to-peak sensitivity of all the array elements is shown in Fig. 11(c).

### *C. Combined Electrical and Acoustical Crosstalk*

The simulated and measured crosstalk values are shown in Figs. 12(a) and 12(b), respectively. As it can be seen, the measured values of crosstalk were found to be comparable to the simulation results. Maximum measured crosstalk values at the array center frequency were -30.5 dB for the first adjacent element, -32.8 dB for the second adjacent element, -34.4 dB for the third adjacent element, and -40.1 dB for the fourth adjacent element; which denote satisfactory but not ideal element-to-element isolation in accordance to the suggested maximum crosstalk design guideline of < -35 dB for phased arrays with a linear configuration [11], [26].

This article has been accepted for publication in a future issue of this journal, but has not been fully edited. Content may change prior to final publication. Citation information: DOI 10.1109/TUFFC.2019.2906134, IEEE Transactions on Ultrasonics, Ferroelectrics, and Frequency Control



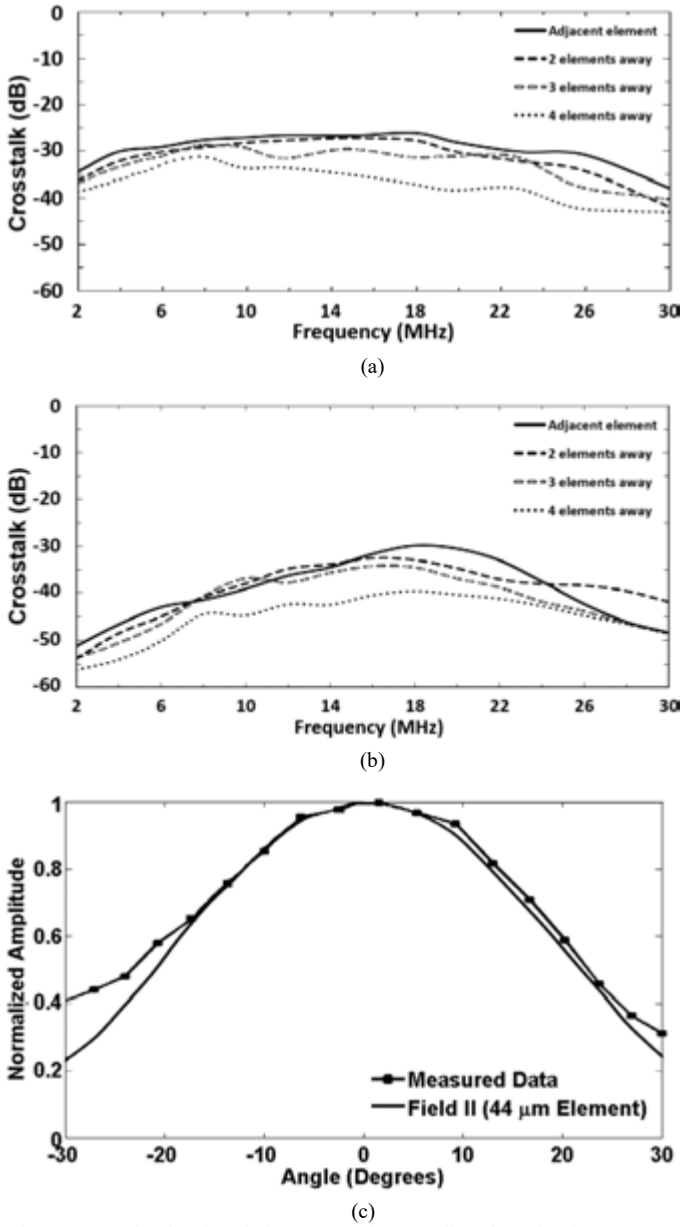


Fig. 12. (a) Simulated and (b) measured crosstalk values for four nearest neighboring elements in the array. (c) Simulated and measured one-way azimuthal directivity response of representative array element 37.

The relatively high crosstalk values for the first and second adjacent elements could be attributed to two main factors: 1. Acoustical cross-coupling between consecutive elements in the 2-2 array composite due to the narrow, 13-μm-wide, epoxy-filled kerfs. 2. Electrical cross-coupling between consecutive signal electrodes on the flexible printed circuit having a pitch of only 50 μm.

### *D. Single-Element Azimuthal Directivity Response*

The simulated and measured one-way azimuthal directivity response of representative array element 37 are shown in Fig. 12(c). The measured -6 dB directivity was approximately ±22°. Since the isolation between consecutive elements was not ideal, the effective element width (44 μm) was 19% larger than the actual element width of 37 μm. A similar result was reported by Ritter *et al.* [27] of an effective element width 16% larger than the actual element width for a 30-MHz linear array with maximum crosstalk < -30 dB and -6 dB directivity of ±20°. Likewise, Chiu *et al.* [28] reported a -6 dB directivity of approximately ±20° for a 20-MHz phased array with maximum crosstalk < -28 dB.

### *E. Array Transducer Imaging*

The acquired image of the custom-made fine-wire phantom is shown in Fig. 13(a). As it can be seen, the three wires were clearly visible with reasonable image quality, especially the middle one located at the elevation natural focal distance. Faint artifacts were observed mostly to the left and right sides of the three wires due to the presence of sidelobes in the ultrasound beam. Implementing apodization could have reduced the amplitude of such sidelobes; however, this would have increased the main lobe width, consequently degrading spatial resolutions [29].

Faint artifacts were also observed on the front of the wires mainly due to thickness irregularities of the matching layers as well as slight wire reverberation and misalignment with respect to the array transducer elevation aperture. Plots of the axial and lateral line spread functions for the middle wire are shown in Figs. 13(b) and 13(c), respectively.

The measured full-width half-maximum (FWHM) spatial resolutions were approximately 90 μm and 420 μm in the axial and lateral directions, respectively. These measurements correlated well with the theoretical axial (80.25 μm) and lateral (450 μm) spatial resolutions, predicted by the well-known equations $R_A = PL/2$ and $R_L = F\# \times \lambda$ [30], where $R_A$ and $R_L$ are the axial and lateral spatial resolutions, respectively; $PL$ is the -6 dB spatial pulse length of the received echo from the previous pulse-echo response measurements (measured -6 dB time pulse length of 0.107 μs corresponds to a -6 dB spatial pulse length of 160.5 μm), $F\#$ is the F-number of the array transducer aperture defined as the ratio of focal distance to aperture dimension [26], and $\lambda$ is the sound wavelength in the transmitting medium.

The acquired images of the custom-made colorectal tissue-mimicking phantom with an inserted 700-μm-diameter stainless steel needle are shown in Fig. 14. Fig. 14(a) shows the needle inserted at a depth of approximately 3 mm and oblique across the array transducer azimuth aperture. Fig. 14(b) shows

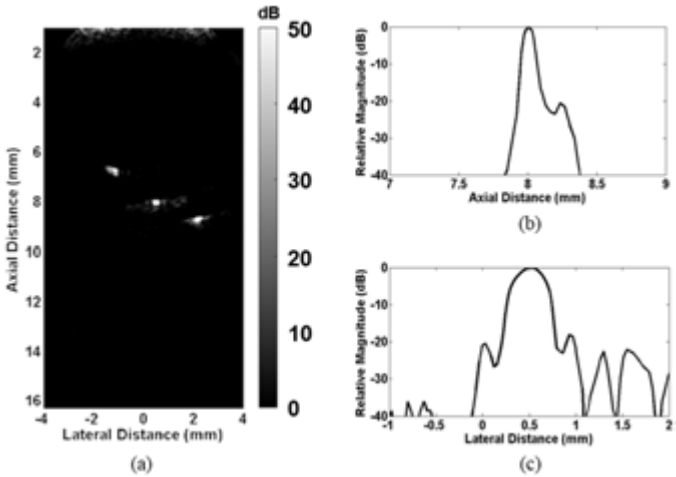


Fig. 13. Imaging of custom-made fine-wire phantom. (a) Acquired image with a dynamic range of 48 dB. (b) Plot of the axial line spread function for the middle wire. (c) Plot of the lateral line spread function for the middle wire.

This article has been accepted for publication in a future issue of this journal, but has not been fully edited. Content may change prior to final publication. Citation information: DOI 10.1109/TUFFC.2019.2906134, IEEE Transactions on Ultrasonics, Ferroelectrics, and Frequency Control



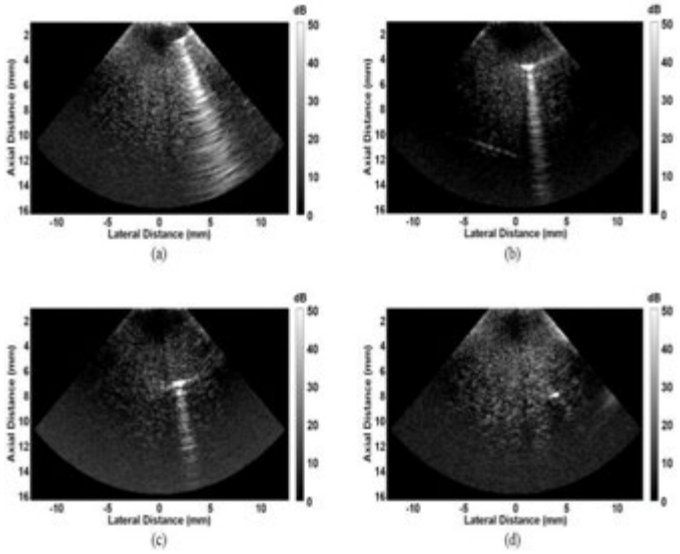


Fig. 14. Imaging of custom-made colorectal tissue-mimicking phantom with inserted stainless steel needle. Images have a dynamic range of 48 dB. (a) Needle inserted at a depth of 3 mm and oblique across the array transducer azimuth aperture. (b) Needle inserted at a depth of 5 mm and oblique across the array transducer azimuth aperture. (c) Needle inserted at a depth of 8 mm and oblique across the array transducer azimuth aperture. (d) Needle inserted at a depth of 8 mm and parallel across the array transducer elevation aperture.

the needle inserted at a depth of approximately 5 mm and oblique across the array transducer azimuth aperture. Fig. 14(c) shows the needle inserted at a depth of approximately 8 mm and oblique across the array transducer azimuth aperture. Fig. 14(d) shows the needle inserted at a depth of approximately 8 mm and parallel across the array transducer elevation aperture.

The acquired images of the custom-made colorectal tissue-mimicking phantom with an inserted piece of 3-mm-diameter polyimide tubing are shown in Fig. 15. Fig. 15(a) shows the cyst resulting from inserting the piece of polyimide tubing at a depth of approximately 5 mm and parallel across the array transducer elevation aperture. Similarly, Fig. 15(b) shows the cyst resulting from inserting the piece of polyimide tubing at a depth of approximately 8 mm and parallel across the array transducer elevation aperture.

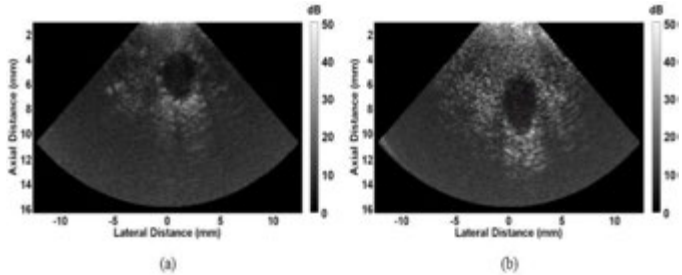


Fig. 15. Imaging of custom-made colorectal tissue-mimicking phantom with inserted piece of polyimide tubing. Images have a dynamic range of 48 dB. (a) Piece of polyimide tubing inserted at a depth of 5 mm and parallel across the array transducer elevation aperture. (b) Piece of polyimide tubing inserted at a depth of 8 mm and parallel across the array transducer elevation aperture.

## VII. Conclusion

This paper described the design, fabrication, and testing of a miniature 15-MHz side-looking phased-array transducer. The 64-element phased-array transducer was fitted inside of a 1.5-m long 10F catheter having an external diameter of only 3.3 mm. The device construction enables its potential integration into a novel robotic surgical instrument that combines endomicroscopy and ERUS.

Standard characterization testing confirmed that the array provides adequate peak-to-peak sensitivity (≥ 100 mV) and spatial resolution (90 μm axially / 420 μm laterally). The relatively high crosstalk (≤ -30 dB) may be reduced in the future with the addition of particles or liquid plasticizer to the kerf filling epoxy to increase attenuation between consecutive elements in the 2-2 composite. Likewise, insertion loss and SNR can be improved by providing the cable assembly with additional shielding and by including impedance transformers or active pre-amplifiers on each channel, respectively.

Finally, acquired images of custom-made colorectal tissue-mimicking phantoms confirmed that the array provides adequate penetration depth (≥ 8.1 mm) and demonstrated its capability to detect solid structures and cysts present in tissue; therefore confirming its potential suitability to provide intraoperative image guidance and tissue characterization during TEM procedures.

## Acknowledgment

The authors are grateful to Mr. Richard Roth from Hitachi Cable America, Dr. Jian Tian from CTS Corporation, and Dr. Ruimin Chen from the Resource Center for Medical Ultrasonic Transducer Technology at USC for their technical suggestions on micro-coaxial cabling, PMN-30%PT composites, and array transducer characterization testing, respectively. The authors also thank the editors and reviewers for their helpful suggestions.

## References

[1] A. Cuschieri, “Technology for minimal access surgery,” *BMJ,* vol. 319, no. 1304, pp. 1-6, Nov. 1999.

[2] V. Ignatov, N. Kolev, A. Tonev, S. Shterev, E. Encheva, T. Kirilova, T. Teneva, and K. Ivanov, “Diagnostic Modalities in Colorectal Cancer – Endoscopy, CT and PET Scanning, Magnetic Resonance Imaging (MRI), Endoluminal Ultrasound and Intraoperative Ultrasound,” *InTech Open Science Open Minds*, pp. 29-51, Mar. 2014.

[3] R. J. Dickinson and R. I. Kitney, “Miniature ultrasonic probe construction for minimal access surgery,” *Phys. Med. Biol.,* vol. 49, no. 16, pp. 3527-3538, Sep. 2004.

[4] T. Cummins, P. Eliahoo, and K. K. Shung, “High-Frequency Ultrasound Array Designed for Ultrasound-Guided Breast Biopsy,” *IEEE Trans. Ultrason. Ferroelectr. Freq. Control,* vol. 63, no. 6, pp. 817-827, June 2016.

[5] Y. Yang, X. Li, T. Wang, P. D. Kumavor, A. Aguirre, K. K. Shung, Q. Zhou, M. Sanders, M. Brewer, and Q. Zhu, “Integrated optical coherence tomography, ultrasound and photoacoustic imaging for ovarian tissue characterization,” *Biomedical Optics Express*, vol. 2, no. 9, pp. 2551-2561, Sep. 2011.

[6] K. Masamune and J. Hong, “Advanced Imaging and Robotics Technologies for Medical Applications,” *Int. J. Optomechatroni.,* vol. 5, no. 4, pp. 299-321, Dec. 2011.

[7] G. Dwyer, P. Giataganas, P. Pratt, M. Hughes, and G. Z. Yang, “A Miniaturized Robotic Probe for Real-Time Intraoperative Fusion of Ultrasound and Endomicroscopy,” in *Proc. IEEE ICRA,* Seattle, WA, USA, 2015, pp. 1196-1201.

[8] B. R. Edelman and M. R. Weiser, “Endorectal ultrasound: Its role in the diagnosis and treatment of rectal cancer,” *Clin. Colon Rectal Surg*., vol. 21, no. 3, pp. 167-177, Aug. 2008.

[9] S. J. Choi, H. S. Kim, S. J. Ahn, Y. M. Jeong, and H. Y. Choi, “Evaluation of the growth pattern of carcinoma of colon and rectum by MDCT,” *Acta Radiol.,* vol. 54, no. 5, pp. 487-492, June 2013.

[10] Y. Chen, K. H. Lam, D. Zhou, W. F. Cheng, J. Y. Dai, H. S. Luo, and H. L. W. Chan, "High-frequency PMN-PT single crystal focusing transducer fabricated by a mechanical dimpling technique," *Ultrasonics*, vol. 53, no. 2, pp. 345-349, Feb. 2013.

[11] R. E. McKeighen, "Design Guidelines for Medical Ultrasonic Arrays," in *Proc. SPIE 3341 Medical Imaging: Ultrasonic Transducer Engineering,* San Diego, CA, USA, 1998, pp. 1-18.

[12] D. M. Pozar, "Transmission Line Theory," in *Microwave Engineering,* 4th ed., Hoboken, NJ, USA: John Wiley & Sons, Inc., 2012, ch. 2, pp.48-94.

[13] J. M. Cannata, J. A. Williams, Q. Zhou, T. A. Ritter, and K. K. Shung, "Development of a 35-MHz Piezo-Composite Ultrasound Array for Medical Imaging," *IEEE Trans. Ultrason. Ferroelectr. Freq. Control*, vol. 53, no. 1, pp. 224-236, Feb. 2006.

[14] C. S. DeSilets, J. D. Fraser, and G. S. Kino, "The Design of Efficient Broad-Band Piezoelectric Transducers," *IEEE Trans. Sonics Ultrason.,* vol. 25, no. 3, pp. 115-125, May 1978.

[15] D. M. Pozar, "Microwave Network Analysis," in *Microwave Engineering,* 4th ed., Hoboken, NJ, USA: John Wiley & Sons, Inc., 2012, ch. 4, pp. 165-227.

[16] R. Chen, N. E. Cabrera-Munoz, K. H. Lam, H. S. Hsu, F. Zheng, Q. Zhou, and K. K. Shung, "PMN-PT Single-Crystal High-Frequency Kerfless Phased Array," *IEEE Trans. Ultrason. Ferroelectr. Freq. Control*, vol. 61, no. 6, pp. 1033-1041, June 2014.

[17] J. A. Jensen, "FIELD: A Program for Simulating Ultrasound Systems," *Med. Biol. Eng. Comp.,* vol.34, no.1, pp. 351-353, 1996.

[18] H. P. Savakus, K. A. Klicker, and R. E. Newnham, "PZT-epoxy piezoelectric transducers: A simplified fabrication procedure," *Materials Res. Bull.,* vol. 16, no. 1, pp. 677-680, June 1981.

[19] H. Wolf, H. Gieser, and L. Maurer, "Transmission Lines on Flexible Substrates with Minimized Dispersion and Losses," in *European Microwave Integrated Circuit Conference,* Nuremberg, Germany, 2013, pp. 448-451.

[20] G. R. Lockwood, D. H. Turnbull, and F. S. Foster, "Fabrication of High Frequency Spherically Shaped Ceramic Transducers," *IEEE Trans. Ultrason. Ferroelectr. Freq. Control*, vol. 41, no. 2, pp. 231-235, Mar. 1994.

[21] J. M. Cannata, J. A. Williams, and K. K. Shung, "A Kerfless 30 MHz Linear Ultrasonic Array," in *Proc. IEEE Ultrason. Symp.*, Rotterdam, The Netherlands, 2005, pp. 109-112.

[22] R. Krimholtz, D. A. Leedom, and G. L. Matthaei, "New equivalent circuits for elementary piezoelectric transducers," *Electronics Letters,* vol. 6, no. 13, pp. 398-399, June 1970.

[23] D. N. Stephens, J. M. Cannata, R. Liu, J. Z. Zhao, K. K. Shung, H. Nguyen, R. Chia, A. Dentinger, D. Wildes, K. E. Thomenius, A. Mahajan, K. Shivkumar, K. Kim, M. O'Donnell, and D. J. Sahn, "The Acoustic Lens Design and *in vivo* Use of a Multifunctional Catheter Combining Intracardiac Ultrasound Imaging and Electrophysiology Sensing*," IEEE Trans. Ultrason. Ferroelectr. Freq. Control*, vol. 55, no. 3, pp. 602-618, Mar. 2008.

[24] J. Lienig and H. Bruemmer, "Electromagnetic Compatibility (EMC)," in *Fundamentals of Electronic Systems Design,* 1st ed., Cham, Switzerland: Springer International Publishing AG, 2017, ch. 6, pp. 147-191.

[25] R. L. Goldberg, C. D. Emery and S. W. Smith, "Hybrid multi/single layer array transducers for increased signal-to-noise ratio," *IEEE Trans. Ultrason. Ferroelectr. Freq. Control*, vol. 44, no. 2, pp. 315-325, Mar. 1997.

[26] K. K. Shung, "Ultrasonic Transducers and Arrays," in *Diagnostic Ultrasound: Imaging and Blood Flow Measurements,* Boca Raton, FL, USA: CRC Press, 2006, ch. 3, sec. 3.6.4, pp. 63-65.

[27] T. A. Ritter, T. R. Shrout, R. Tutwiler, and K. K. Shung, "A 30-MHz Piezo-Composite Ultrasound Array for Medical Imaging Applications," *IEEE Trans. Ultrason. Ferroelectr. Freq. Control*, vol. 49, no. 2, pp. 217-230, Aug. 2002.

[28] C. T. Chiu, B. J. Kang, P. Eliahoo, T. Abraham, and K. K. Shung, "Fabrication and Characterization of a 20-MHz Microlinear Phased-Array Transducer for Intervention Guidance," *IEEE Trans. Ultrason. Ferroelectr. Freq. Control*, vol. 64, no. 8, pp. 1261-1268, Aug. 2017.

[29] C. H. Frazier and W. D. O'Brien, "Synthetic aperture techniques with a virtual source element," *IEEE Trans. Ultrason. Ferroelectr. Freq. Control*, vol. 45, no. 1, pp. 196-207, Jan. 1998.

[30] F. S. Foster, M. Y. Zhang, Y. Q. Zhou, G. Liu, J. Mehi, E. Cherin, K. A. Harasiewicz, B. G. Starkoski, L. Zan, D. A. Knapik, and S. L. Adamson, "A New Ultrasound Instrument for *In Vivo* Microimaging of Mice," *Ultrasound Med. Biol*., vol. 28, no. 9, pp. 1165-1172, June 2002.